



Contents lists available at ScienceDirect

# International Journal of Applied Earth Observations and Geoinformation

journal homepage: [www.elsevier.com/locate/jag](http://www.elsevier.com/locate/jag)

## A new Global Navigation Satellite System (GNSS) based method for urban heat island intensity monitoring

Jorge Mendez-Astudillo<sup>a</sup>, Lawrence Lau<sup>b,c,\*</sup>, Yu-Ting Tang<sup>d</sup>, Terry Moore<sup>e</sup>

<sup>a</sup> International Doctoral Innovation Center, University of Nottingham Ningbo China, China

<sup>b</sup> Department of Civil Engineering, University of Nottingham Ningbo China, China

<sup>c</sup> Department of Land Surveying and Geo-Informatics, The Hong Kong Polytechnic University, Hong Kong, China

<sup>d</sup> School of Geographical Sciences, University of Nottingham Ningbo China, China

<sup>e</sup> The Nottingham Geospatial Institute, the University of Nottingham, UK

### ARTICLE INFO

#### Keywords:

Urban heat island  
GNSS  
GNSS remote sensing  
Zenith tropospheric delay

### ABSTRACT

The Urban Heat Island (UHI) effect occurs when an urban area experiences higher temperatures than its rural surrounding because of heat being absorbed by built structures and heat being released by anthropogenic sources. UHIs can cause adverse effects to human health and increase energy consumption used for cooling buildings. Therefore, it is important to monitor accurately the UHI effect. The intensity of UHIs are usually monitored using satellite imagery, airborne sensors, and surface temperature sensors. Satellite imagery can cover a large area but requires a clear sky to obtain good images. Moreover, airborne sensors are expensive and also require a clear sky to obtain good data. A large network of surface temperature sensors is required to monitor the UHI of an entire region, which can also be expensive. In this paper, we present a three-step algorithm to monitor UHI intensity using data from Global Navigation Satellite Systems (GNSS). The advantages of using GNSS data to monitor the UHI effect are the increased availability of observation data, high temporal resolution and high geographical resolution. The first step of the algorithm is the calculation of *a priori* environmental parameters (*i. e.*, water vapour partial pressure, troposphere height, surface pressure, and the vertical profile of refractivity) from radiosonde data. The second step is the calculation of temperature from GNSS data. The last step is the UHI intensity computation. The algorithm presented in this paper has been tested and validated using publicly available GNSS and meteorological data from Los Angeles, California, USA. The validation of the algorithm is done by comparing the UHI intensity estimated from the algorithm with temperature data obtained from weather stations. In the validation, the proposed algorithm can achieve an accuracy of 1.71 °C at 95 % confidence level.

### 1. Introduction

The urban heat island (UHI) effect occurs when urban regions experience warmer temperatures than their rural surroundings (Roth, 2013). The main causes of the UHI are the heat absorbed by the built structures and the anthropogenic heat sources in a city (Roth, 2013). It is important to monitor UHI intensity (UHII) because they exacerbate heat waves and can cause adverse effects to the environment such as increases in ground-level ozone (Memon et al., 2009; Rizwan et al., 2008). An increasing population with a large and denser built area leads to a higher UHI intensity. (Golden et al., 2007) and increased energy consumption due to the increased demand for artificial air-conditioning of buildings (Kikegawa et al., 2003). As a result, more electrical energy is

produced and more greenhouse gasses are emitted due to the combustion of fossil fuels (Yu and Hien, 2006). This increases smog production, as well as contributing to the increased emission of pollutants from power plants (Shahmohamadi et al., 2011). Furthermore, UHI influences the quality of life and human well-being in urban areas (Schwarz et al., 2011). For instance, warmer temperatures in cities can cause discomfort, and an increase in morbidity and mortality rates (Memon et al., 2009; Rizwan et al., 2008). The UHI effect can also alter other environmental quality measures, create stress on water resources because of an increased demand for water in the city (Jauregui, 1997), decrease air quality (Jauregui, 1997) and reduce biodiversity (Schwarz et al., 2011).

Three techniques are currently used to monitor the UHI intensity: a

\* Corresponding author at: Department of Civil Engineering, University of Nottingham Ningbo China, China.

E-mail addresses: [Lawrence.Lau@nottingham.edu.cn](mailto:Lawrence.Lau@nottingham.edu.cn), [lsg-lawrence.lau@polyu.edu.hk](mailto:lsg-lawrence.lau@polyu.edu.hk) (L. Lau).

<https://doi.org/10.1016/j.jag.2020.102222>

Received 5 April 2020; Received in revised form 25 June 2020; Accepted 17 August 2020

Available online 6 September 2020

0303-2434/© 2020 The Author(s). Published by Elsevier B.V. This is an open access article under the CC BY license (<http://creativecommons.org/licenses/by/4.0/>).

network of ground-based temperature sensors (Jauregui, 1997; Ramamurthy and Sangobanwo, 2016); satellite data (Mohegh et al., 2018; Tanaka et al., 2005; Vahmani and Ban-Weiss, 2016) and airborne instruments (Grimmond et al., 2010). UHI intensity is monitored with ground-based sensors by measuring the difference of temperature between sensors within an urban area and in a nearby rural area (Jin, 2012). The main disadvantage of surface temperature sensors is that a dense network of sensors is needed to cover a metropolitan area leading to increased monitoring costs.

Satellite imaging and airborne instruments have the advantage of covering a large geographical area. However, clear-sky conditions are required to obtain accurate data. Satellite images are obtained from remote sensing products such as the LANDSAT satellite. The Thematic Mapper and the Enhanced Thematic Mapper of LANDSAT have been used to monitor UHI intensity in different cities such as Shanghai (Li et al., 2012) or Rio de Janeiro (de Faria Peres et al., 2018). Images are scarce because clear skies are required to obtain high quality images. Furthermore, the use of airborne instruments increases the cost of monitoring UHI intensity. Examples of other remote sensing instrument used to monitor the UHI is the Moderate Resolution Imaging Spectroradiometer (MODIS) which is used with a four-parameter diurnal temperature cycle model (Lai et al., 2018) to monitor the UHI in 354 Chinese cities. MODIS temperature data has also been used to monitor the urban heat island effect across biomes in the USA (Imhoff et al., 2010). Furthermore, the MODIS atmospheric profile product has been used to monitor the UHI in four mega-cities in North America (Hu and Brunzell, 2015). The Urban Heat Island in Los Angeles, California has been studied using meteorological data (Ramamurthy and Sangobanwo, 2016) Also, the UHI in LA has been studied using the Weather Forecast Research model and MODIS data in order to study the effect of vegetation to the UHI in LA (Vahmani and Ban-Weiss, 2016). Moreover, the effect of roof albedo to the UHI in LA has been studied (Mohegh et al., 2018).

In this paper we present a novel method of monitoring UHI intensity using ground-based observation data from Global Navigation Satellite Systems (GNSS). The algorithm is based on the relationship between the tropospheric delay caused by the atmosphere and the environmental variables at the site of measurement. Ground-based GNSS data has been used to monitor environmental variables such as precipitable water (Bevis et al., 1994; Jin et al., 2014; Vaquero-Martínez et al., 2017). This algorithm presents the use of ground based GNSS data to estimate temperature and monitor the UHI intensity.

The advantages of GNSS data compared to other remote sensing satellite products are the availability of GNSS data, these signals are available in all weather conditions and there are many satellites available in a given position at all times (Jin, 2012). The second advantage is that GNSS data has a higher temporal resolution, because it can be collected and processed at different time intervals. Particularly, GNSS data can be obtained and processed in real-time. Another advantage is that because of miniaturization, GNSS sensors are currently embedded in many hand-held devices such as smartphones, recent research has focused on the potential that raw GNSS data collected with smartphones has in surveying and positioning (Håkansson, 2019). Therefore, GNSS sensors are widely available allowing for the building of a dense network with high spatial resolution at relatively low cost.

In Section 2 of this paper, the data used for validation of the algorithm is described, In Section 3 of this paper, the algorithm developed to monitor the UHI intensity from GNSS data is presented. The UHI intensity (UHII) in the testing location is presented in Section 4. The output of the algorithm is compared with the UHII found with surface meteorological data at the same locations as the GNSS stations in order to validate the output of the algorithm. In Section 5, discussion and conclusions are given.

## 2. Materials and methods

### 2.1. Study area

Los Angeles (LA) is the second most populous city and metropolitan area of the United States of America (USA). LA is a coastal city in the west coast of the USA, it is located across a broad coastal plain between mountains and the Pacific Ocean. The LA climate is typically classified as semi-arid or subtropical Mediterranean (Csb) based on Köppen-Geiger’s classification (Ramamurthy and Sangobanwo, 2016). In terms of built environment layout, the city is composed of a series of widely dispersed settlements loosely connected to downtown (Britannica, 2019). LA has been chosen as a test site because of the dispersed distribution of the settlement and the fact that there are different geographical conditions across the settlement, including mountains, the Pacific Ocean and desert. In LA metropolitan area there are many GNSS and meteorological stations covering most of the territory and data are easily available for both, GNSS and meteorological stations.

### 2.2. Data used to monitor the UHI intensity

GNSS data is the input to the algorithm to estimate the temperature from Zenith Tropospheric Delay (ZTD) and to monitor the UHII. For validation purposes, the temperature estimated with the algorithm is compared to the meteorological data obtained from meteorological stations near the GNSS stations. Therefore, the test site, the GNSS and the meteorological data used to test and validate the algorithm are described in the following sub-sections.

#### 2.2.1. GNSS data in LA

The source of GNSS data in is the International GNSS Service (IGS) which provides observation data and other products such as navigation data and precise ephemeris. In total, there are 16 IGS GNSS stations in the LA metropolitan area located in different environments such as mountains, near bodies of water and near the desert. However, only 5 stations are used to test the algorithm because these GNSS stations are close to a meteorological station (less than 1 km away).

Table 1 shows the details of the GNSS stations in LA metropolitan area used to test the algorithm. The first column of Table 1 indicates the IGS station code, followed by the columns indicating the latitude, longitude and altitude of the station as reported by the IGS. Furthermore, the fifth column indicates the municipality where the station is located. The last column indicates whether the station is in a rural-type area (R) or in an urban-type environment (U). The classification is done before the data is processed using satellite images of the surroundings of the station. Data from 5 years, 2014–2019 has been used to test the algorithm.

#### 2.2.2. Meteorological data from LA

The meteorological data used for the validation of the algorithm is obtained from the U.S National Centres for Environmental Information (NCEI) of the National Oceanic and Atmospheric Administration (NOAA) which provides access to climate databases run by different authorities in the US and Canada (<https://www.ncdc.noaa.gov/cdo-web>). Daily averages, maximum temperature, and minimum temperature are typically provided. However, data is not consistently available

**Table 1**  
IGS GNSS stations used to test the algorithm in LA metropolitan area.

IGS code	Latitude	Longitude	Height	Municipality	Type
HOLP	33.92	−118.16	−6.71	Hollydale	U
SPK1	34.05	−118.64	440.13	Saddle Peak	R
WIDC	33.93	−116.39	445.04	Sky Valley	R
LBCH	33.79	−118.2	−27.58	Long Beach	U
TORP	33.79	−118.33	−5.22	Torrance	U

at every station during every day of the study. The data used for this study comes from 5 stations deployed around the city, the exact locations and details of the meteorological stations are presented in Table 2.

Data from year 2014-2019 has been processed. All data is collected at a standard height of 2 m above the surface. The first column of Table 2 indicates the code assigned by NOAA, then the latitude, longitude and height of the stations are reported. The fourth column indicates the municipality where the station is located, and the last column indicates the type of area where the station is located following the same classification scheme used for the GNSS stations.

### 3. Algorithm to monitor the UHII from GNSS data

The intensity of the UHI (UHII) is defined by the difference between a temperature in an urban area and one in its surrounding rural area. The algorithm is divided in 4 steps:

- 1 Data collection simultaneously in an urban and a rural area.
- 2 Processing of GNSS data to obtain the ZTD and location of the station. The Precise Point Positioning technique (Lau et al., 2003; Zumberge et al., 1997) is used (PPP).
- 3 Calculation of temperature using ZTD in the urban and the rural station
- 4 Computation of the UHII.

#### 3.1. Classification of the type of environment around the station

Urban areas are densely populated and densely constructed (Memon et al., 2009). In urban areas, there are anthropogenic sources of heat, such as the means of transportation and air conditioning units, among others. In contrast, a rural area has few built structures, is mostly covered by nature and the numbers and types of anthropogenic heat sources are reduced. Usually rural and urban areas are attached to each other, with rural areas found outside the city or urban area. (Memon et al., 2009).

In satellite imagery where a pixel of the picture represents several km, an urban area will be typically a city, and a rural area, its surroundings. However, when the remote sensing resolution is increased, an urban-like or rural-like area can be defined within a city. Examples of urban-like and rural-like areas in the Los Angeles (LA) metropolitan area are shown in Fig. 1 a) and Fig. 1 b), respectively.

Fig. 1 a) shows a rural-like area, in this case, a golf course in Carson, California. The golf course is a big green area with no built structures. It is surrounded by an expressway, which is a source for anthropogenic heat caused by the moving vehicles. However, the space is open air so the contribution to the UHI is minimum. The golf course is also surrounded by low density housing areas, which contain gardens as well and have a low population density. In contrast, Fig. 1 b) encircles an urban area, which is in downtown LA. The urban area contains many high rising buildings very close to each other, as well as streets

**Table 2**  
Location of the meteorological stations in the Los Angeles metropolitan area used to validate the algorithm.

NOAA code	Latitude	Longitude	Height	Municipality	Type
USW00003167	33.92278	-118.3342	19.2	Hawthorne airport	R
USW00093134	34.0236	-118.2911	54.6	Los Angeles downtown	U
USW00023174	33.938	-118.3888	29.6	Los Angeles International Airport	R
USW00023129	33.8116	-118.1463	9.4	Long Beach Airport	U
USC00047326	33.8342	-118.3759	43.3	Redondo Beach	R

containing vehicles (source of anthropogenic heat). The downtown area is surrounded by other urban areas, which also have many built structures. The classification of the type of area is done visually from satellite imagery by inspecting characteristics of the surroundings of the stations or locations.

Fig. 2 shows the surroundings of GNSS stations: SPK1 and WIDC which are both considered as rural stations. Fig. 3 shows the surroundings of the GNSS stations HOLP, LBCH and TORP are considered as urban stations.

The stations depicted in Fig. 2 are surrounded by nature. SPK1 is on the mountains to the north of Los Angeles and WIDC is to the west close to the desert. Since there are not built structures and a few sources of anthropogenic heat, the stations are considered as in rural areas.

The stations depicted in Fig. 3: TORP, LBCH and HOLP are in urban areas. TORP is near an airport in Torrance, the stations are close to many built structures and sources for anthropogenic heat such as highways and the airport. The station LBCH is surrounded by built structures, it is located in Long Beach. The station HOLP is located in Hollydale and it is surrounded by built structures, however the structures are not densely packed as in the case of LBCH.

#### 3.2. Estimation of ZTD

Ground-based GNSS observation data described in Table 1 has been processed with RTKLIB to obtain the location of the receivers and the ZTD. RTKLIB is an open source positioning software, developed by T. Takatsu (<http://www.rtklib.com/>). It can implement different positioning techniques, among them the Precise Point Positioning (PPP) method, which can be computed in either static or kinematic mode. The PPP technique is implemented with an Extended Kalman Filter (EKF) (Tolman, 2008) which allows the estimation of parameters such as ZTD using observation data, navigation data and precise ephemeris (Zumberge et al., 1997). The estimation of parameters can achieve a cm accuracy (Gao, 2006). RTKLIB is used because a previous study has shown that the estimations are done with high precision (Mendez Astudillo et al., 2018).

RTKLIB required the precise ephemeris, clock and navigation data which are obtained from the IGS final products. A value for ZTD was estimated with a 30 s interval because that is the interval of data availability. 5 years (2014–2019) of data have been processed.

#### 3.3. Algorithm to calculate temperature from GNSS data

The algorithm developed to calculate temperature from GNSS data is shown in the block diagram in Fig. 4. The algorithm requires *a priori* values for the height of the troposphere ( $S$ ), air pressure at the place of measurement ( $P$ ) and the water vapor partial pressure ( $e$ ) at the site of measurement to compute the profile of the refractivity. These values are obtained from radiosonde data and are called the universal parameters.

##### 3.3.1. Calculation of universal parameters

**3.3.1.1. Height of the troposphere ( $S$ ).** The height of the troposphere  $S$  is calculated using GNSS data and radiosonde data as described in Mendez Astudillo et al. (2020). The height of the troposphere  $Z_{trop}$  is calculated using the criteria for the first and second lapse rate tropopause (LRT1 and LRT2) defined by the World Meteorological Organization (WMO) and radiosonde data: the LRT1 is defined as the lowest level at which the lapse rate (change of temperature with height) decreases to  $2^\circ\text{C} / \text{km}$  or less, provided also that the averaged lapse rate between this level and levels within the next 2 km vertically does not exceed  $2^\circ\text{C} / \text{km}$ . If above the LRT1 the average lapse rate between any level and all higher levels with 1 km exceeds  $3^\circ\text{C} / \text{km}$ , then a second tropopause (LRT2) is defined. LRT2 may be either within or above the 1 km layer (WMO, 1957). The path of the GNSS signal in troposphere is defined as the

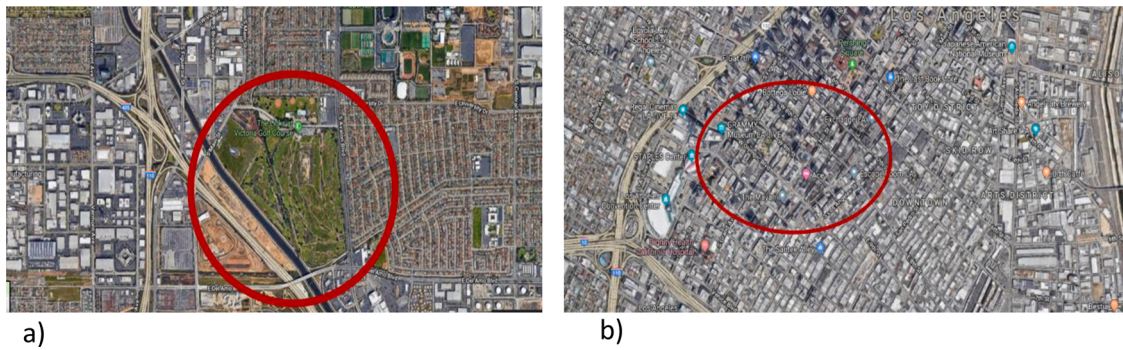


Fig. 1. Examples of a) a rural-type area, and b) an urban-like area, in LA.



Fig. 2. Surroundings of GNSS stations SPK1 and WIDC, considered rural stations.



Fig. 3. Surroundings of the stations: TORP, LBCH and HOLP considered urban stations.

height of LRT2. The height of LRT2 has been calculated with radiosonde data from stations covering all the latitudes of the world. (from latitudes in  $-90^\circ$  to  $90^\circ$  with a  $5^\circ$  step). Fig. 5 shows a diagram indicating the path of the GNSS signal from the satellite to the receiver and the location of LRT1 and LRT2 within the troposphere.

3.3.1.2. Pressure ( $P$ ). The pressure is obtained from radiosonde sounding, it is considered a constant, as its annual fluctuation is

negligible.

3.3.1.3. Water vapor partial pressure at different heights  $e(z)$ . The water vapor partial pressure  $e(z)$  is calculated using Antoine's model and temperatures from radiosonde data at the different heights ( $z$ ). Defined with the following equation (Tolman, 2008):

$$e(z) = \frac{10^{A - \frac{B}{C+T(z)}}}{0.75} \quad (1)$$

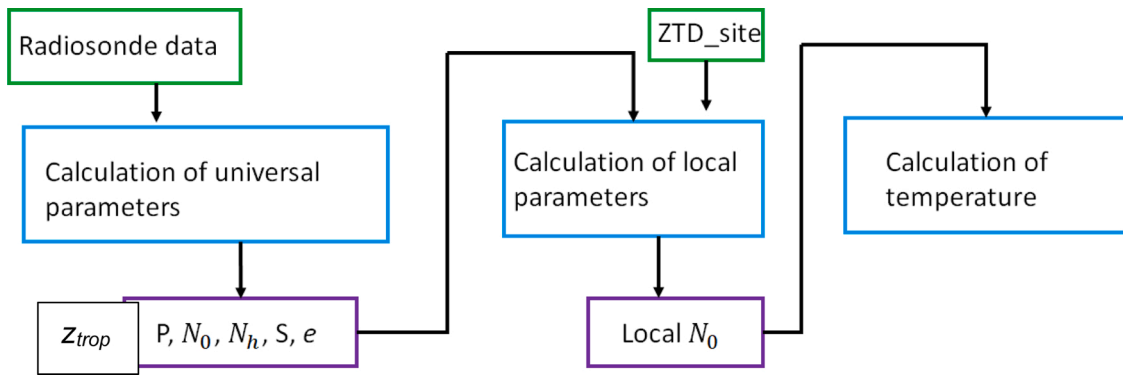


Fig. 4. Block diagram of the algorithm developed to estimate temperature from GNSS data.

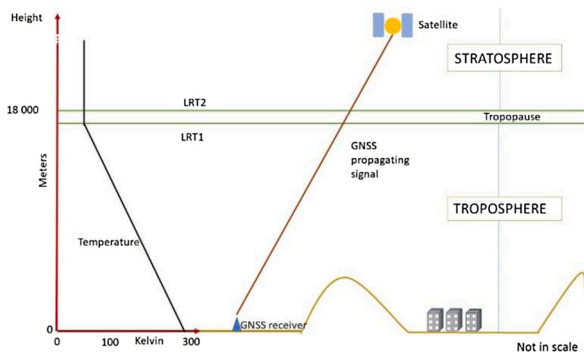


Fig. 5. Path of GNSS signal and profile of the temperature in the troposphere.

where A, B and C are Antoine’s constants (A = 8.071, B = 1730.63 and C = 233.43). T(z) is the temperature in Kelvin (Tolman, 2008). Equation 1 is valid for temperatures greater than 0 °C and lower than 100 °C. It is assumed that urban temperatures in the metropolitan areas under study are between that range most of the time. Negative temperatures are assumed to yield 0 hPa of water vapor partial pressure.

### 3.3.2. Calculation of local parameters

The tropospheric delay is related to the environment conditions through the refractivity of the troposphere. The refractivity N of the troposphere is defined as: (Essen and Froome, 1951).

$$N = k_1 \cdot \frac{P - e}{T} + k_2 \cdot \frac{e}{T} + k_3 \cdot \frac{e}{T^2} \quad (2)$$

where the empirically calculated constants  $k_1 = 77.6$ ,  $k_2 = 72$  and  $k_3 = 3.75 \cdot 10^5$  (Thayer, 1974). P is the pressure of the air at the point of measurement, e is the water vapor partial pressure and the T is the temperature in kelvins. The profile of the refractivity against height has been calculated using radiosonde data and Eq. 2 at different heights. 10 years of radiosonde data have been processed from 2009 to 2019 (Radiosonde USM00072376 located in the coordinates latitude = 35.05°, longitude=-111°, height = 2179 m) and the following relation has been empirically derived:

$$N = N_0 \exp^{-N_h z} \quad (3)$$

where  $N_0$  is the refractivity at height equals to 0 m,  $N_h$  is the ratio of change of the refractivity with altitude.  $Z_{trop}$  is the height at which the measurement is taken. The troposphere causes a delay to the signal in the zenith direction ZTD (in m) which can be expressed as an integral of the total refractivity N along propagation path s from receiver r to satellite w (Hofmann-Wellenhof et al., 2008):

$$ZTD = 10^{-6} \int_r^w N ds \quad (4)$$

A local  $N_0$  ( $N_{0\_local}$ ) is found using  $N_h$ ,  $Z_{trop}$  (height of the tropopause), the altitude of the receiver ( $Z_{rec}$ ) and the ZTD in Eq. 5:

$$N_{0\_local} = \frac{ZTD}{q \int_{Z_{rec}}^{Z_{trop}} \exp^{N_h z} dz} \quad (5)$$

$N_{0\_local}$  is the value of the refractive index near the surface of the place of measurement.

3.3.2.1. Calculation of temperature. The temperature of the site is calculated by putting zero to the equation of refractivity (Eq. 2) and solving the quadratic equation:

$$N_{0\_local} T^2 - T(k_1 P - (k_1 + k_2)e) - k_3 e = 0 \quad (6)$$

### 3.3.3. Calculation of the UHII intensity (UHII) from GNSS data

The UHI intensity is calculated by subtracting the temperature at an urban station from the temperature at a rural station. An average daily temperature is obtained per year. An average for the 5 year is obtained in order to test the algorithm. The algorithm is validated by comparing the UHII obtained with GNSS data with the UHII obtained with meteorological data. The UHII in LA has been calculated using the temperature estimated with ground based GNSS observation data in an urban and a rural station. The temperatures estimated with the algorithm in the rural stations: SPK1 and WIDC have been subtracted to the temperatures estimated with GNSS data from urban stations: HOLP, LBCH and TORP. Eq. 7 shows the calculations:

$$UHII_{HOLP} = T_{gnss}(HOLP) - T_{gnss}(SPK1) \quad (7)$$

$$UHII_{LBCH} = T_{gnss}(LBCH) - T_{gnss}(WIDC)$$

$$UHII_{TORP} = T_{gnss}(TORP) - T_{gnss}(SPK1)$$

$$UHII_{TORP} = T_{gnss}(TORP) - T_{gnss}(WIDC)$$

where  $T_{gnss}(\text{Location})$  is the temperature in °C obtained with the algorithm at the chosen location. 5 years of data have been processed, every day a value of T has been found and they have been averaged to find a single T per day. The averaged T has been used to estimate the UHII shown in Eq. 7.

### 3.4. UHII obtained with meteorological data

Meteorological data described in Fig. 2 has been processed to calculate the UHII in LA. The meteorological stations in urban areas are in Los Angeles Downtown (LAD) and Long Beach (LBC). The stations in rural-like areas are in the Hawthorne Municipal Airport (HAW), Los Angeles International Airport (LAX) and Redondo Beach (RBC) as described in Table 2. The UHI intensity from meteorological data has been calculated using the relations shown in Equation 8.

$$UHII_{dw} = T_{met}(lad) - T_{met}(haw)$$

$$UHII_{dx} = T_{met}(lad) - T_{met}(lax)$$

$$UHII_{dr} = T_{met}(lad) - T_{met}(rbc)$$

$$UHII_{lw} = T_{met}(lbc) - T_{met}(haw)$$

$$UHII_{lx} = T_{met}(lbc) - T_{met}(lax)$$

$$UHII_{lr} = T_{met}(lbc) - T_{met}(rbc) \tag{8}$$

The UHII obtained with GNSS and meteorological data are presented

in Section 4.

#### 4. Results

In this section, the intensity of the UHI in LA obtained with GNSS and meteorological data are shown. Fig. 6 shows the UHII estimated with ground based GNSS observation data from 2014–2019.

Spring in the northern hemisphere has been defined as days of the year 60–151, summer has been defined as days of the year 152–243. Autumn has been defined as days of the year 244–334 and winter has been defined as days of the year 1–60 and 335–365. During the summer months, the intensity of the UHI increases while during the winter

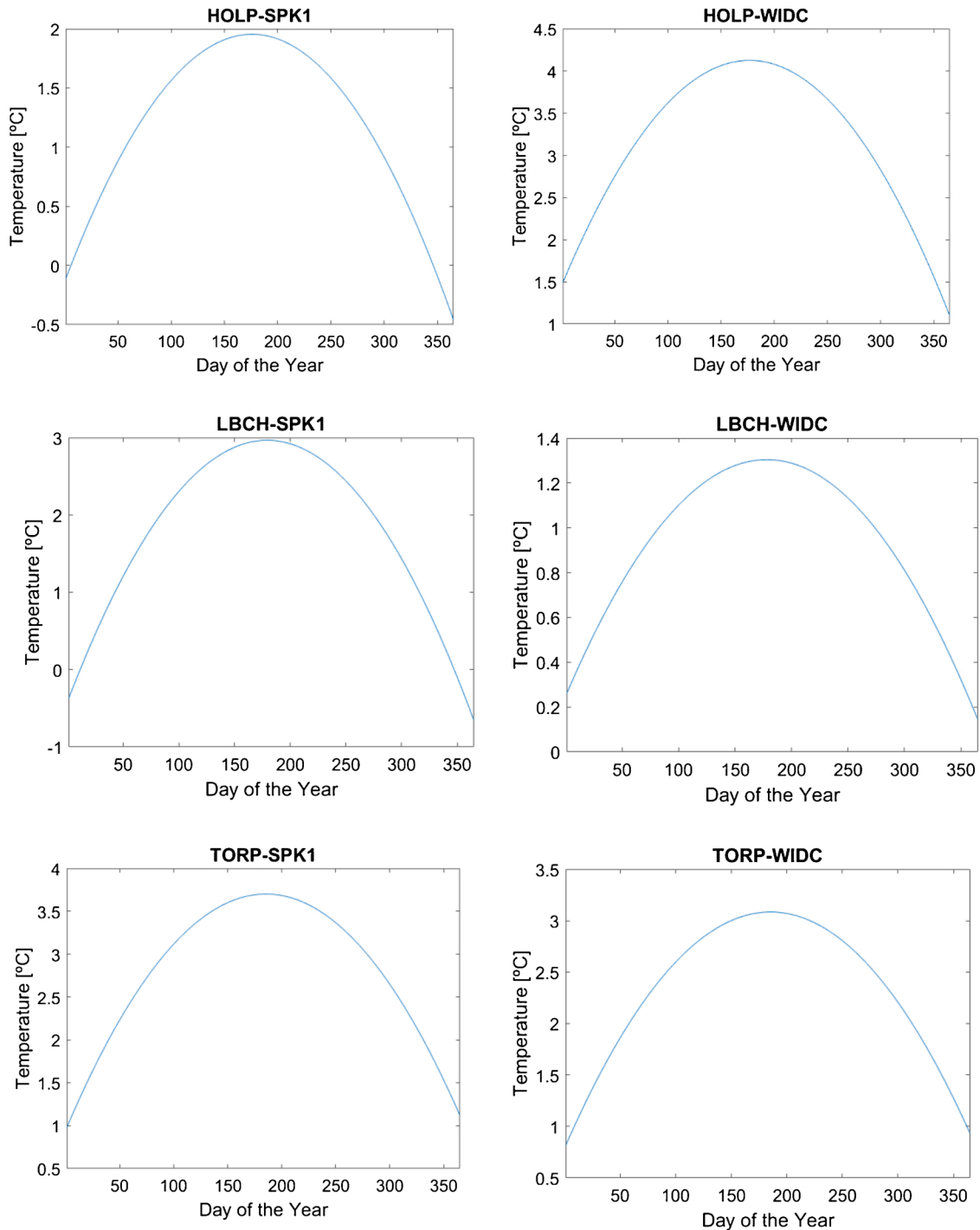


Fig. 6. UHI intensity estimated with ground based GNSS observation data in three locations in LA metropolitan area; see Eq. 6.

months the UHII is lower. The yearly average intensity and the average intensity with GNSS data from each season (spring, summer, autumn and winter) with data from years 2014–2019 are shown in Table 3. The seasonal data each year has been averaged and a single seasonal average has been obtained. Table 3 shows the average UHII in °C using 5-year data and seasonal data.

#### 4.1. UHII calculated with meteorological data

An average of the intensity of the UHI, a maximum and a minimum value each day has been obtained with meteorological data. Fig. 7 shows these values for the 6 pairs of selected stations in LA.

Fig. 7 shows that in all cases, during the summer the difference of temperature between the urban and the rural stations is bigger than during the winter. The UHII for stations in Los Angeles Downtown and Hawthorne Airport have a very similar environment, both are in rural-like areas, therefore, the intensity of the UHI between these stations is around 2 °C and the minimum and maximum values are around 1 °C on top or bottom of the average value. The average UHI intensity for each station with data from 5 years is shown in Table 4. Moreover, the average intensity for each season of the year is presented in Table 4.

### 5. Validation of results

GNSS receivers are located 1.5–2 meters above the ground in order to reduce multipath effect by the ground. Therefore, the temperature estimated with the algorithm is used to monitor the UHI intensity in the urban canopy layer because the air temperature around the receiver is estimated. Meteorological stations measure the air temperature at 1.5–2 meters above the ground. Therefore, the results presented in Fig. 7 and Table 4 measure the UHI intensity in the urban canopy layer.

Thus, the validation of the algorithm has been carried out by comparing the UHII determined by GNSS data (UHII\_gnss) with the UHII calculated from temperature sensors at weather stations (UHII\_met). The difference of the intensity at a given day of the year (Diff\_UHII(DOY)) has been compared by using the following simple calculation:

$$Diff\_UHII(DOY) = UHII\_gnss(DOY) - UHII\_met(DOY) \tag{9}$$

The mean value of the differences is used as the indicator of the quality of the estimation. The first comparison is done using all available data, then the comparison of the differences using data from different seasons is done. The average difference of the results obtained with GNSS and with meteorological data are shown in Table 6. The RMS value of the differences is used to validate the algorithm. Also, the maximum and minimum value of UHI intensity found with GNSS data and with meteorological using all data and using seasonal data are shown in Table 7.

All the results obtained with GNSS data shown in Fig. 6, are within the range of the UHII found with meteorological data as shown in Fig. 7. The shape of the graphs obtained with both methods is very similar, during the summer months the intensity of the UHI increases in comparison with the winter months. The UHI intensity has been calculated with different stations which are located in similar environments and

**Table 3**  
Average intensity and average intensity from each season obtained using GNSS data from 2014-2019.

Pair of stations	GNSS Intensity [°C]				
	5-year data	Spring	Summer	Autumn	Winter
HOLP-SPK1	1.06	1.07	0.91	1.21	1.06
HOLP-WIDC	1.03	1.06	0.85	1.14	1.06
LBCH-SPK1	1.85	1.92	1.75	1.87	1.86
LBCH-WIDC	1.83	1.93	1.71	1.85	1.85
TORP-SPK1	0.92	0.93	0.80	1.02	0.92
TORP-WIDC	0.81	0.88	0.59	0.90	0.86

nearby.

The 6 pairs of meteorological and GNSS data used for validation purposes are related by location as described in Table 5.

The average differences between UHII from GNSS data and meteorological data are shown in Table 6 where all differences are below 3 °C.

The Root Mean Square of the differences between the UHII obtained with GNSS data and meteorological data are shown in Table 7. The RMS value for the 5-year data and for each of the seasons are shown in Table 7.

The accuracy of the UHII determination is 1.71 °C at a 95 % confidence level using the whole 5-year data.

### 6. Discussion and conclusion

The algorithm is based on the estimation of temperature from GNSS data, which is achieved because of the relation between the refractivity of the troposphere and the environmental variables (pressure, water vapor partial pressure and temperature) at the site of measurement and the relation of the refractivity of the troposphere and the ZTD presented in this paper. Furthermore, the ZTD is defined as the integral over the path of the signal affected by the refractivity of the troposphere. Therefore, it is necessary to know the height of the top of the troposphere at the point of measurement. Radiosonde data and the WMO definition of the second lapse rate tropopause are used to calculate the height of the top of the troposphere.

Radiosonde data are used to calculate the profile of the refractivity of the troposphere as described in this paper. Moreover, values of pressure and water vapor partial pressure are estimated from radiosonde data. The values estimated from radiosonde data and the ZTD estimated with a PPP implementation, in this case RTKLIB, are the input to the algorithm. The output of the algorithm is the temperature at the site of measurement. In order to monitor the UHI intensity, it is necessary to estimate the temperature from GNSS data at an urban and a rural location simultaneously. GNSS data from the 6 selected locations in LA has been used as input to the algorithm to monitor the UHI effect.

The algorithm here presented demonstrates the possibility of using GNSS data to monitor the UHI intensity. Ground-based GNSS data has the following advantages: it works in all weather conditions, it is widely available as GNSS constellations are designed to cover the earth at all moments and it can be collected with hand-held receivers such as smartphones which can allow to build dense sensor networks without increasing the cost. Also, GNSS data has a very high temporal resolution and it can be processed in real-time or near-real-time. This algorithm shows that GNSS data can be used in urban climate studies in the micro- and meso- scale.

There are three main challenges to the algorithm that have been overcome. The first is the definition of urban and rural areas. Since, the algorithm allows to increase the spatial resolution of the estimation of temperature, the classification of an urban and rural station is made in terms of the amount of anthropogenic heat sources surrounding the GNSS and meteorological station. A high-density sensor network of GNSS receivers allows the monitoring of the UHI at low cost and high spatial resolution.

The second challenge is the difference of heights where the UHII is estimated and measured. All meteorological stations have a weather sensor which is located 2 m above the ground. Therefore, the UHI intensity is measured with weather stations data within the canopy layer. The GNSS stations are located at different altitudes. Therefore, during validation, the effect of height in temperature has been taken into account. According to WMO definition, every 1 km of altitude there is one 6.5 °C of difference. After the adjustment of temperature due to altitude, the temperature reported by the weather stations and estimated from GNSS data are at the same altitude and can be compared.

The third challenge of the algorithm is the estimation of water vapor partial pressure *e* since it cannot be measured with sensors. The value of *e* must be modeled using temperatures at different heights obtained with

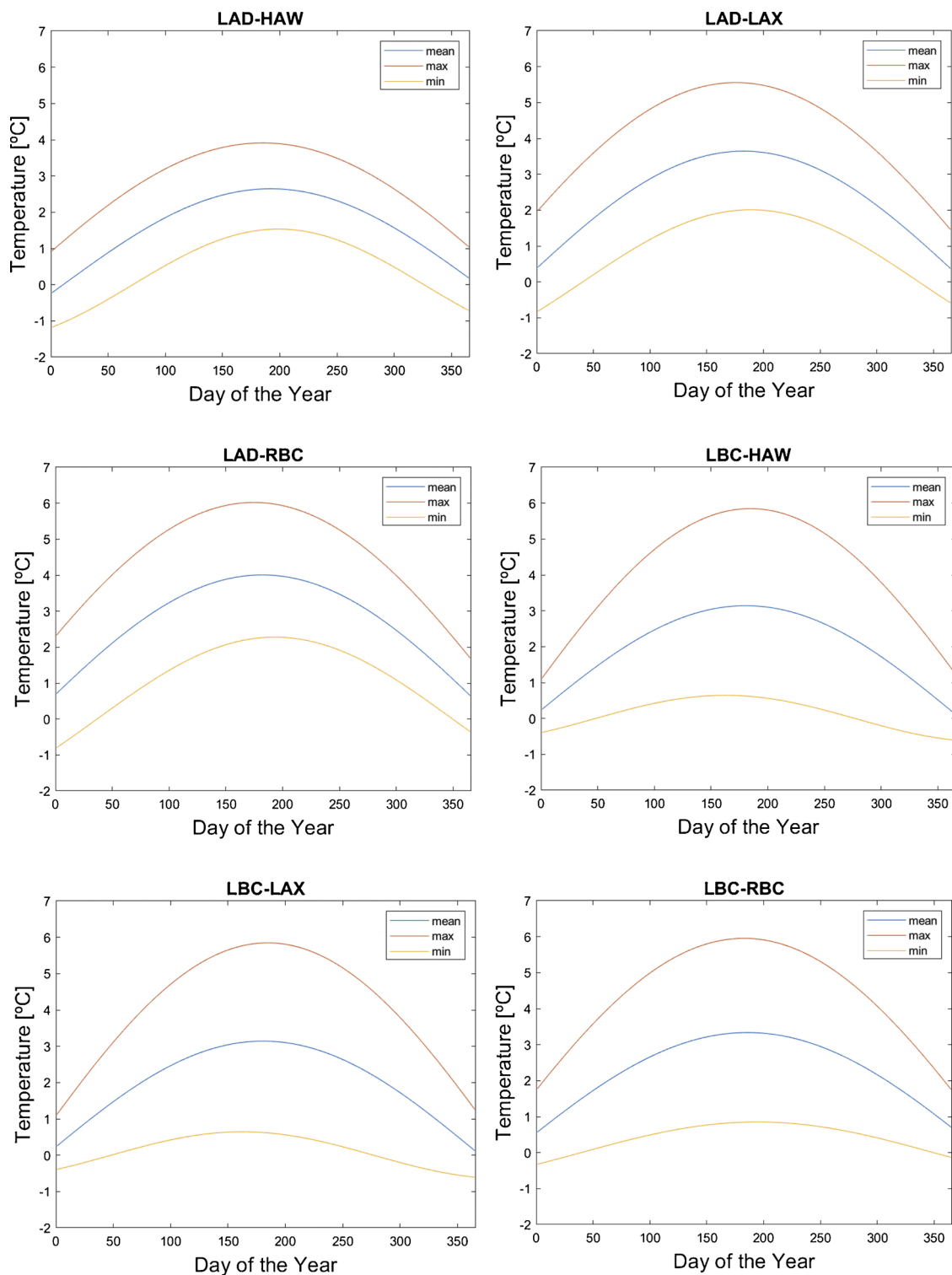


Fig. 7. UHI calculated from 3 pairs of meteorological stations.

radiosondes. Therefore, only two directly measured values are available per day, one at 00:00 UTC and one at 12:00 UTC. The value of  $e$  at different times can be obtained using interpolation techniques.

The output of this novel algorithm has been validated by comparing the UHI obtained from the algorithm and from temperature sensors available at weather stations in the Los Angeles metropolitan area. The average difference is less than 3 °C for all pairs of stations studied. In all cases, during the summer is when the intensity of the UHI is the highest and the difference between the results of the algorithm and

meteorological data are the lowest. According to the RMS of the differences, all pairs of stations except for UHI 3 (Table 5) are less than 2.5 °C. Overall, the proposed algorithm has achieved an average accuracy of 1.71 °C at 95 % confidence level.

It has been shown that during spring and winter, the difference of the UHI obtained with GNSS data and the measured UHI with temperature data is lower than during other seasons, because during the summer and autumn it is typically dry season. Therefore, the water vapor partial pressure is not accurately modeled for those seasons. The discrepancies

**Table 4**

Yearly UHII for 6 pairs of meteorological stations in LA metropolitan area using 5 years data and using seasonal data.

Intensity [°C]					
Pair of stations	5-year data	Spring	Summer	Autumn	Winter
LAD-HAW	1.68	1.62	2.85	1.63	0.59
LAD-LAX	2.47	2.53	3.98	2.18	1.17
LAD-RBC	2.59	2.58	3.95	2.86	1.17
LBC-HAW	1.27	1.3	2.3	1.23	0.5
LBC-LAX	2.07	2.52	3.98	2.18	1.18
LBC-RBC	1.12	2.58	3.95	2.77	0.94

**Table 5**

Relation of meteorological and GNSS pairs.

	Meteorological data	GNSS data
UHII1	LAD-HAW	HOLP-SPK1
UHII2	LAD-LAX	HOLP-WIDC
UHII3	LAD-RBC	TORP-SPK1
UHII4	LBC-HAW	LBCH-SPK1
UHII5	LBC-LAX	LBCH-WIDC
UHII6	LBC-RBC	TORP-WIDC

**Table 6**

Average differences between UHII obtained with GNSS data and meteorological data at the 6 selected locations in LA.

UHII difference [°C]					
Pair of stations	5-year data	Spring	Summer	Autumn	Winter
UHII1	1.22	1.27	1.18	1.26	1.115
UHII2	2.18	2.31	2.14	2.15	2.04
UHII3	2.75	3.05	2.77	2.11	2.74
UHII4	1.55	1.69	1.44	1.54	1.56
UHII5	1.71	1.81	1.74	1.93	1.54
UHII6	1.73	1.91	1.65	1.90	1.54

**Table 7**

RMS of the differences between UHII obtained with GNSS data and meteorological data at the 6 selected locations in LA.

RMS [°C]					
Pair of stations	5-year data	Spring	Summer	Autumn	Winter
UHII1	1.45	1.46	1.42	1.49	1.37
UHII2	2.33	2.43	2.29	2.3	2.21
UHII3	3.22	3.5	3.24	2.64	3.18
UHII4	1.65	1.75	1.57	1.67	1.61
UHII5	2.12	2.19	2.08	2.35	2
UHII6	2.08	2.23	1.96	2.2	2.04

between the UHII estimated with the algorithm and the UHII obtained from meteorological stations can be attributed to the lack of water vapor partial pressure data, difference of altitude between the GNSS and meteorological station and GNSS processing. The algorithm can be implemented in real- or near-real- time if GNSS data and inputs to the algorithm are found in that time frame. It can be used to monitor the diurnal cycle of the UHI.

**Declaration of interests**

The authors declare that they have no known competing financial interests or personal relationships that could have appeared to influence the work reported in this paper.

**CRedit authorship contribution statement**

**Jorge Mendez-Astudillo:** Investigation, Data curation, Software,

Writing - original draft. **Lawrence Lau:** Conceptualization, Supervision, Funding acquisition, Writing - review & editing. **Yu-Ting Tang:** Methodology, Writing - review & editing. **Terry Moore:** Supervision, Writing - review & editing.

**Acknowledgments**

This work was supported by financial support from the International Doctoral Innovation Centre, Ningbo Education Bureau, Ningbo Science and Technology Bureau, and the University of Nottingham. This work was also supported by the UK Engineering and Physical Sciences Research Council [grant number [EP/L015463/1]. We would like to thank two anonymous reviewers whose comments and suggestions were of great value for this contribution.

**References**

Bevis, M., Businger, S., Chiswell, S., Herring, T.A., Anthes, R.A., Rocken, C., et al., 1994. GPS meteorology: mapping zenith wet delays onto precipitable water. *J. Appl. Meteorol.* 33, 379–386.

Britannica, E., 2019. Los Angeles, California, United States. Retrieved from. <https://www.britannica.com/place/Los-Angeles-California>.

de Faria Peres, L., de Lucena, A.J., Rotunno Filho, O.C., de Almeida França, J.R., 2018. The urban heat island in Rio de Janeiro, Brazil, in the last 30 years using remote sensing data. *Int. J. Appl. Earth Obs. Geoinf.* 64, 104–116.

Essen, L., Froome, K.D., 1951. Dielectric constant and refractive index of air and its principal constituents at 24,000 mc./s. *Nature* (167), 512–513.

Gao, Y., 2006. GNSS solutions: precise point positioning and its challenges. *Inside GNSS (November/December)*, 16–18.

Golden, J.S., Carlson, J., Kaloush, K.E., Phelan, P., 2007. A comparative study of the thermal and radiative impacts of photovoltaic canopies on pavement surface temperatures. *Sol. Energy* 81 (7), 872–883. <https://doi.org/10.1016/j.solener.2006.11.007>.

Grimmond, C.S.B., Roth, M., Oke, T.R., Au, Y.C., Best, M., Betts, R., et al., 2010. Climate and more sustainable cities: climate information for improved planning and management of cities. *Environ. Sci.* 1, 247–272.

Håkansson, M., 2019. Characterization of GNSS observations from a Nexus 9 Android tablet. *Gps Solut.* 23 (21) <https://doi.org/10.1007/s10291-018-0818-7>.

Hofmann-Wellenhof, B., Lichtenegger, H., Wasle, E., 2008. *GNSS-Global Navigation Satellite Systems GPS, Glonass, Galileo and more.* Springer, Vienna, Austria.

Hu, L., Brunzell, N.A., 2015. A new perspective to assess the urban heat island through remotely sensed atmospheric profiles. *Remote Sens. Environ.* 158, 393–406.

Imhoff, M.L., Zhang, P., Wolfe, R.E., Bounoua, L., 2010. Remote sensing of the urban heat island effect across biomes in the continental USA. *Remote Sens. Environ.* 114, 504–513.

Jauregui, E., 1997. Heat island development in Mexico city. *Atmos. Environ.* 31 (22), 3821–3831.

Jin, M.S., 2012. Developing an index to measure urban heat island effect using satellite land skin temperature and land cover observations. *J. Clim.* 25 (18), 6193–6201. <https://doi.org/10.1175/jcli-d-11-00509.1>.

Jin, S., Cardellach, E., Xie, F., 2014. *GNSS remote sensing theory. Methods and Applications.* Springer.

Kikegawa, Y., Genchi, Y., Yoshikado, H., Kondo, H., 2003. Development of a numerical simulation system toward comprehensive assessments of urban warming countermeasures including their impacts upon the urban buildings' energy-demands. *Appl. Energy* 76, 449–466. [https://doi.org/10.1016/s0306-2619\(03\)00009-6](https://doi.org/10.1016/s0306-2619(03)00009-6).

Lai, J., Zhan, W., Huang, F., Voogt, J., Bechtel, B., Allen, M., et al., 2018. Identification of typical diurnal patterns for clear-sky climatology of surface urban heat islands. *Remote Sens. Environ.* 217, 203–220.

Lau, L., Pattinson, M., Sheridan, K., 2003. Adapted precise point positioning within galileo development and validation activities. In: Paper Presented at the GNSS 2003 The European Navigation Conference. Graz, Austria. 22–25 April 2003.

Li, Y.-y., Zhang, H., Kainz, W., 2012. Monitoring patterns of urban heat islands of the fast-growing Shanghai metropolis, China: using time-series of Landsat TM/ETM+ data. *Int. J. Appl. Earth Obs. Geoinf.* 19, 127–138.

Memon, R.A., Leung, D.Y.C., Liu, C.-H., 2009. An investigation of urban heat island intensity (UHII) as an indicator of urban heating. *Atmos. Res.* 94 (3), 491–500. <https://doi.org/10.1016/j.atmosres.2009.07.006>.

Mendez Astudillo, J., Lau, L., Tang, Y.T., Moore, T., 2018. Analysing the zenith tropospheric delay estimates in on-line precise point positioning (PPP) services and PPP software packages. *Sensors (Basel)* 18 (2). <https://doi.org/10.3390/s18020580>.

Mendez Astudillo, J., Lau, L., Tang, Y.T., Moore, T., 2020. A novel approach for the determination of the height of the tropopause from ground-based GNSS observations. *Remote Sens.* 12 (293) <https://doi.org/10.3390/rs12020293>.

Mohegh, A., Levinson, R., Taha, H., Gilbert, H., Zhang, J., Li, Y., et al., 2018. Observational evidence of neighborhood scale reductions in air temperature associated with increases in roof albedo. *Climate* 6 (98), 19. <https://doi.org/10.3390/cli6040098>.

Ramamurthy, P., Sangobanwo, M., 2016. Inter-annual variability in urban heat island intensity over 10 major cities in the United States. *Sustain. Cities Soc.* 26, 65–75.

- Rizwan, A.M., Dennis, L.Y.C., Liu, C., 2008. A review on the generation, determination and mitigation of Urban Heat Island. *J. Environ. Sci.* 20 (1), 120–128. [https://doi.org/10.1016/s1001-0742\(08\)60019-4](https://doi.org/10.1016/s1001-0742(08)60019-4).
- Roth, M., 2013. Urban heat island. In: Fernando, H.J.S. (Ed.), *Handbook of Environmental Fluid Dynamics*, Vol. II. Taylor & Francis Group, pp. 143–159.
- Schwarz, N., Lautenbach, S., Seppelt, R., 2011. Exploring indicators for quantifying surface urban heat islands of European cities with MODIS land surface temperatures. *Remote Sens. Environ.* 115 (12), 3175–3186. <https://doi.org/10.1016/j.rse.2011.07.003>.
- Shahmohamadi, P., Che-Ani, A.I., Maulud, K.N.A., Tawil, N.M., Abdullah, N.A.G., 2011. The impact of anthropogenic heat on formation of urban heat island and energy consumption balance. *Urban Stud. Res.* 2011, 1–9. <https://doi.org/10.1155/2011/497524>.
- Tanaka, Y., Shibata, S., Gotoh, K., 2005. Appearance characteristic analysis of heat island phenomenon by using satellite remote sensing and GIS. *Simposium IGARS 3 (1855-1858)*, 25–29.
- Thayer, G., 1974. An improved equation for the radio refractive index of air. *Radio Sci.* 9, 211–222. <https://doi.org/10.1029/RS009i010p00803>.
- Tolman, B.W., 2008. GPS precise absolute positioning via Kalman filtering. In: *Paper Presented at the ION GNSS 21st International Technical Meeting of the Satellite Division*. Savannah, GA.
- Vahmani, P., Ban-Weiss, G.A., 2016. Impact of remotely sensed albedo and vegetation fraction on simulation of urban climate in WRF-urban canopy model: a case study of the urban heat island in Los Angeles. *J. Geophys. Res. Atmos.* (121), 1511–1531. <https://doi.org/10.1002/2015JD023718>.
- Vaquero-Martínez, J., Antón, M., Ortiz de Galisteo, J.P., Cachorro, V.E., Costa, M.J., Román, R., et al., 2017. Validation of MODIS integrated water vapor product against reference GPS data at the Iberian Peninsula. *Int. J. Appl. Earth Observ. Geoinf.* (63), 214–221. <https://doi.org/10.1016/j.jag.2017.07.008>.
- WMO, 1957. *Lapse Rate Tropopause*. World Meteorological Organization.
- Yu, C., Hien, W.N., 2006. Thermal benefits of city parks. *Energy Build.* 38 (2), 105–120. <https://doi.org/10.1016/j.enbuild.2005.04.003>.
- Zumberge, J.F., Heflin, M.B., Jefferson, D.C., Watkins, M.M., Webb, F.H., 1997. Precise point positioning for the efficient and robust analysis of GPS data from large networks. *Geophys. Res. Lett.* 24, 5005–5017.